Research Article | Vol. 13, No. 6 / 1 Jun 2022 / Biomedical Optics Express 3295
Biomedical Optics EXPRESS

Portable boom-type ultrahigh-resolution OCT with an integrated imaging probe for supine position retinal imaging

ZHENGYU DUAN,[1,2,5] KAI HUANG,[3] ZHONGZHOU LUO,[1] KE MA,[1] GENGYUAN WANG,[1] XIAODONG HU,[1] JINZE ZHANG,[1] XIAOLING LUO,[1] YUANCONG HUANG,[1] GANGJUN LIU,[4] XIAOYAN DING,[1,5] PENG XIAO,[1,6] AND JIN YUAN[1,7]

[1]State Key Laboratory of Ophthalmology, Zhongshan Ophthalmic Center, Sun Yat-sen University, Guangdong Provincial Key Laboratory of Ophthalmology and Visual Science, Guangzhou 510060, China
[2]School of Biomedical Engineering, Sun Yat-sen University, Guangzhou 510006, China
[3]School of Computer Science and Engineering, Sun Yat-sen University, Guangzhou 510006, China
[4]Shenzhen Bay Laboratory, Shenzhen 518132, China
[5]the authors contributed equally to this paper
[6]xiaop29@mail.sysu.edu.cn
[7]yuanjincornea@126.com

Abstract: To expand the clinical applications and improve the ease of use of ultrahigh-resolution optical coherence tomography (UHR-OCT), we developed a portable boom-type ophthalmic UHR-OCT operating in supine position that can be used for pediatric subjects, bedridden patients and perioperative conditions. By integrating the OCT sample arm probe with real-time iris display and automatic focusing electric lens for easy alignment, coupling the probe on a self-locking multi-directional manipulator to reduce motion artifacts and operator fatigue, and installing the OCT module on a moveable cart for system mobility, our customized portable boom-type UHR-OCT enables non-contact, high-resolution and high-stability retinal examinations to be performed on subjects in supine position. The spectral-domain UHR-OCT operates at a wavelength of 845 nm with 130 nm FWHM (full width at half maximum) bandwidth, achieving an axial resolution of ≈2.3μm in tissue with an A-line acquisition rate up to 128 kHz. A high-definition two-dimensional (2D) raster protocol was used for high-quality cross-sectional imaging while a cube volume three-dimensional (3D) scan was used for three-dimensional imaging and *en-face* reconstruction, resolving major layer structures of the retina. The feasibility of the system was demonstrated by performing supine position 2D/3D retinal imaging on healthy human subjects, sedated infants, and non-sedated awake neonates.

1. Introduction

Optical coherence tomography (OCT) is an emerging technology for a wide range of biomedical applications including organ imaging, real-time surgical guidance, and high-resolution imaging of biological specimens [1–8]. The eye is composed of a series of transparent structures and there are many lamellar structures with micrometer thickness in both the anterior and posterior segments [9,10]. Thus, OCT is widely used as a noncontact and noninvasive imaging technique for acquiring high-resolution, cross-sectional, in vivo images of ocular tissues [11–14]. It is becoming a routine imaging tool and adopted as the gold standard in the diagnosis of many ophthalmic diseases [15,16]. However, since most commercialized clinical available OCT platforms are static, table-mounted machines, they can only scan cooperative subjects in an upright seated position, placing their head on a headrest, guided by a fixation target and holding their eyes open for several seconds [17,18]. Thus, these tabletop stationary OCT devices and

#456435 https://doi.org/10.1364/BOE.456435
Journal © 2022 Received 17 Feb 2022; revised 26 Apr 2022; accepted 29 Apr 2022; published 10 May 2022

Biomedical Optics EXPRESS

their imaging procedures are not practical for non-cooperative infants, young children and supine subjects like bedridden patients and patients undergoing surgery.

Retinal diseases, such as retinopathy of prematurity (ROP) and age-related macular degeneration (AMD), are among the main causes of visual impairment in pediatrics [19,20]and bedridden elderly, respectively [21,22]. Subtle changes less than a couple of micrometers could occur in the retina during early onset and progression of these retinal diseases [23,24]. High-resolution retinal imaging providing detailed structural and functional information is crucial for early disease diagnosis and blindness prevention. In current clinics, retinal imaging modalities like binocular indirect ophthalmoscope and handheld digital fundus camera e.g. RetCam (Massie Laboratories, Inc., USA) are available for bedridden adults, young children and infants, providing fundus photography with good reproducibility for retinal diseases diagnosis and neonatal screening [25,26]. Nevertheless, they could not provide in-depth cross-sectional and three-dimensional (3D) volume information. Thus, there is an emerging need of point of care bedside OCT imaging for these populations, motivating the development of portable OCT systems with integrated miniaturized/handheld imaging probes.

To address the clinical needs of bedside supine OCT imaging, various portable [27], armature mounted [28] or handheld OCT instruments [29] have been developed and clinically applied. Armature mounted Heidelberg Spectralis with Flex Module OCT (Heidelberg Engineering GmbH, Germany) suspend the OCT system over the subject and can be used with cooperative or anesthesia subjects in supine position, but these bulky devices are not practical for daily bedside or incubator imaging [30]. With a miniaturized imaging probe, handheld OCT systems have shown better suitability for supine position imaging especially for pediatric applications. Currently, the only commercially available handheld OCT system Envisu C-Class (Leica Microsystems, Germany) could be used on supine subjects. But its relatively low A-line scanning rate (32 kHz) leads to the compromise between the image acquisition time and the field of view (FOV), and difficulties in providing high quality 3D volume images [31]. By integrating faster scanner, real-time *en-face* imaging and on-probe display, Song et al improved the operator's experience and scanning efficiency, achieving faster 3D and wide-field imaging of human retina [32]. Ergonomic handheld OCT probe design was optimized by Viehland et al for pediatric and supine imaging [33]. Recently, Ni et al applied a novel optical design with advanced double aspheric lens, achieving non-contact handheld 105°ultra-wide-field retinal imaging [34]. The feasibility and repeatability of these commercial and lab prototype for imaging supine subjects and infants were also demonstrated in different clinical environments [35,36]. All these technological advancements have increased the performances of handheld OCTs, offering better imaging modalities for the early detection and treatment response evaluation in pediatric eye diseases [37], Which have also led OCT technology to more widespread use in infants and children, making it an integral part in pediatric eye diseases management [38].

Although current handheld OCT devices are more compact and flexible by minimizing hardware components on the probe, they still suffer limitations associated with motion artifacts and relatively low imaging quality. During handheld OCT imaging operation, operators always need to rest one hand on the subject's forehead for stable lesion localization with fingers opening the eye of anesthetized subjects and the other hand holding the imaging probe, which inevitably induces the relative motion between the probe and the eye, causing motion artifacts and spatial distortion of OCT images, especially during continuous operations [33]. Studies have shown that compared with traditional table-mounted machines, normal handheld instruments on average generate images with lower repeatability and reproducibility, and require more attempts by the operator [23]. Moreover, normal handheld OCT systems not only make operators fatigued, but also need more operating experience to successfully acquire satisfactory images, especially on pediatric subjects.

Biomedical Optics EXPRESS

In this paper, we described the development and initial clinical application of a customized portable boom-type spectral-domain UHR-OCT system with an integrated imaging probe for supine position imaging. An OCT sample arm probe was designed incorporating with a real-time iris camera and an automatic focusing electric lens for easy alignment. To resolve the motion artifacts and reduce operator fatigue during imaging, the OCT probe was installed on a self-locking flexible manipulator. The whole system was placed on a portable cart, ensuring easy movement of the system for point of care bedside imaging. Imaging was performed on healthy human subjects, young children under sedation, and non-sedated awake neonates, demonstrating the feasibility of the system for non-contact high-resolution retinal images in supine position.

2. Materials and methods

2.1. Optical design and instrumentation

As illustrated in Fig. 1(a), our customized portable boom-type UHR-OCT is a SD-OCT (Spectral-Domain OCT) system. The laser source used is a broadband super luminescent diode (SLD, Superlum, cBLMD-850-HP, Cork, Ireland) centered at a wavelength of 850 nm with 165 nm FWHM (Full Width at Half Maximum) bandwidth. After passing through an isolator used to protect the light source from back reflections, the OCT light is equally split into the sample arm and the reference arm of the OCT interferometry by a 50:50 fiber coupler (Thorlabs, TW850R5A2, Newton, NJ, USA). The light of the sample arm then goes to our integrated imaging probe, in which the laser beam is collimated with a fiber collimator (CL2, Thorlabs, PAF-X-11-B, Newton, NJ, United States), passing through an electronically tunable lens designed for autofocus (EL-10-30-C, Optotune, Dietikon, Switzerland), reflected on the galvanometric x-y scanners (Gx, Gy, Cambridge Technology, 6210H set, Bedford, MA, United States), and then relayed by the scan lens (L2, f = 100mm, Edmund Optics, NT45-806, Barrington, NJ, United States) and the ocular lens (OL, Volk optical Inc. 60D, UK) for retinal imaging. The working distance of the probe is ~13 mm. The power of incident light on the human eye is adjusted to 750 μW, below the maximum permissible exposure dictated by ANSI (American National Standard for Ophthalmics—Light Hazard Protection for Ophthalmic Instruments) [39]. To ensure easy alignment during imaging, an iris camera (3206, LuoKe LRCP, Shenzhen, China) having a resolution of 256×256 pixels is installed to the OCT imaging probe with a long-pass dichroic mirror (DM1, Thorlabs, DMLP650, Newton, NJ, United States) inserted after the scanning lens. The integrated iris camera lens (L3) working together with the ocular lens (OL) focus the ocular surface image on the iris camera. In the reference arm, the laser beam is collimated by a fiber collimator (CL1, Thorlabs, PAF-X-7-B, Newton, NJ, United States), passing through a neutral-density filter (NF, Thorlabs, NDC-25C-4M, Newton, NJ, United States) for reference signal control, dispersion compensation prisms (BK7 glass) and focused on a mirror by a focusing lens (L1, f = 100mm, Edmund optics, NT45-806, Barrington, NJ, United States). The reference mirror and the focusing lens are installed on a translational stage for the optical pathlength adjustment of the reference arm, which is matched with the sample arm to its focal position. Two fiber polarization controllers with a loop diameter of 18 mm (FPC020, Thorlabs, Inc, United States) were installed to match the polarization state between the sample and reference arm. The light reflected from the subject's retina in the sample arm and the mirror in the reference arm are collected, combined and sent to the OCT spectrometer (Wasatch Photonics, Cobra-S, United States). The spectrum of the interference signal is acquired with a maximum speed of 128,000 A-lines per second, transferred using the image acquisition board (National Instruments, PCIe-1433, Austin, TX, United States) and processed by our self-developed LabVIEW program running on a computer with Windows 10.

The 3D mechanical design of the integrated OCT imaging probe is shown in Fig. 1(b). The final assembled probe weighs around 500g with a dimension of 20×8×5cm. As shown in Fig. 1(c), the integrated imaging probe is mounted on the end of a manipulator (V7, GLO, Guilin,

Biomedical Optics EXPRESS

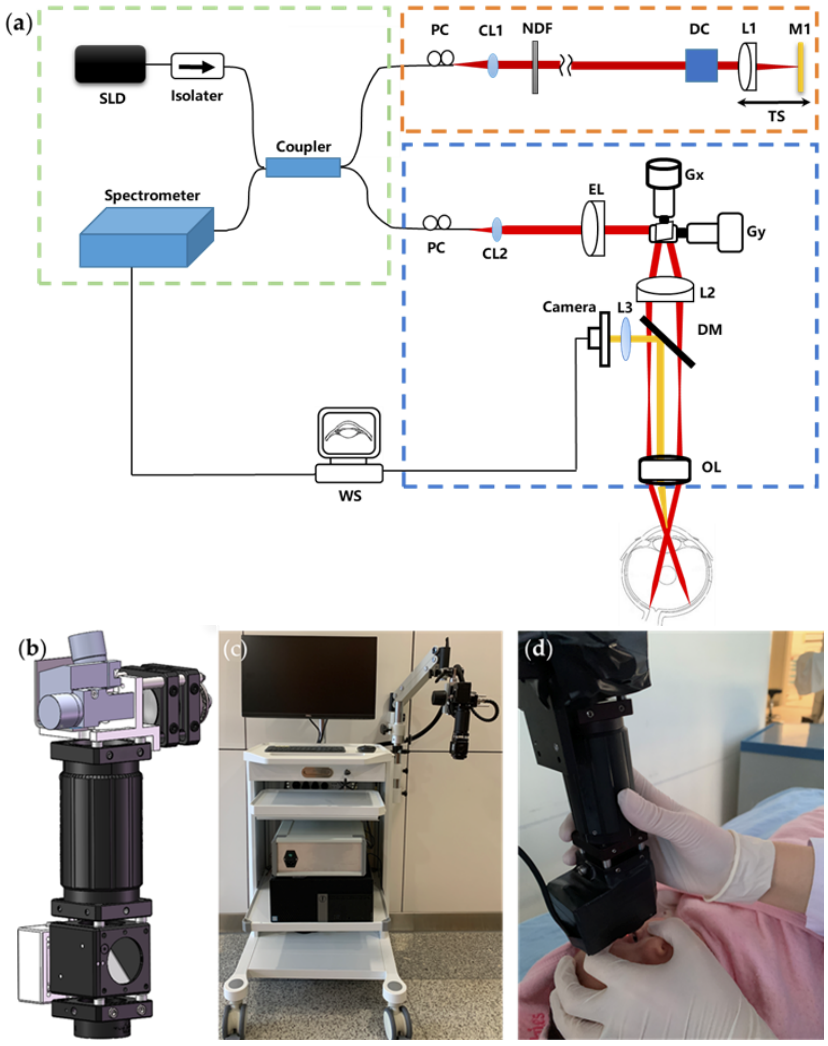

Fig. 1. Schematic and photo of the portable boom-type UHR-OCT. (a) Schematic of the system, SLD: super luminescent diode, CL: collimator, NF: neutral-density filter, DC: Dispersion Compensation prisms, L: lens, G: Galvano scanner, TS: translational stage, WS: work station, EL: electronically tunable lens, PC: polarization controller, DM: dichroic mirror, BS: beam splitter, OL: ocular lens. (b) Main components layout of the probe (c) Photo of the system and (d) Clinical imaging of an infant with novel portable boom-type UHR-OCT.

Biomedical Optics EXPRESS

China). The tension on the manipulator is adjustable to maintain a smooth operation, and with correctly tightness setting according to the probe weight, the manipulator could be self-locked in any position and direction within its adjusting range. The multi-directional manipulator has a maximum horizontal movement range of 100 cm on the installing side to ensure its extension over the examination bed. On the vertical direction, the probe has a rough adjustment range of 50cm by the manipulator arm and a fine adjustment range of 50mm through the manually controlled slideway in the manipulator end. The multi-directional end joint of the manipulator also allows a 360° tilt of the probe to adapt to different eye positions during imaging. The operator could hold the lens tube of the imaging probe by a single hand for alignment and use the other hand to gently open the eye and manipulate the eye position of the examined subjects (needed for pediatric examinations). The flexibility, self-locking and multi-directional traits of the manipulator allow the operator to easily align the probe over the eye of the subjects while maintaining the probe stability to minimize the movement artifacts. Thus, the imaging probe could potentially accommodate patients in different positions like upright, incline sitting or supine position. The laser source, the reference arm, the spectrometer and the computer of the UHR-OCT system are all placed on a moveable medical cart with the manipulator installed on the side of the cart as in Fig. 1(c), ensuring easy movement of the system to adapt to multiple point of care bedside imaging scenarios. The probe is connected with flexible communication cables and optical fibers. A foot switch pedal (TFS-1, TAYB, Shenzhen, China) is connected to the system to easily launch the image acquisition since both hands of the operator would be occupied for imaging alignment. The final system footprint is 0.5m×0.5m with a height of 1.4 m. A photograph demonstrating the imaging of a sedated infant in supine position is shown in Fig. 1(d).

2.2. System characterization

Figure 2(a) shows the measured spectrum of the light source in our system. With the center wavelength of 850 nm with 165 nm bandwidth, the theoretical axial resolution of the system should be ≈1.9μm in the air, nevertheless, as the profile of the laser spectrum was not perfectly Gaussian and the fiber optic components will inevitably limit the available bandwidth, thus the effective axial resolution of the UHR-OCT system would be weakened [40]. The measured wavelength by the spectrometer is 845 nm with 130 nm FWHM bandwidth in Fig. 2(a). In order to obtain the real axial resolution, the axial point spread function (PSF) was measured by imaging a mirror [41]. In Fig. 2(b), the axial resolution of our UHR-OCT module was measured to be ≈3.2μm in the air, corresponding to ≈2.3μm in tissue (cornea and retina) with a refractive index of 1.38 [42]. Figure 2(c) shows the system sensitivity test as a function of imaging depth. The signal to noise ratio (SNR) was measured using a silver mirror as the imaged object without the ocular lens. The maximum SNR of 94 dB was measured ~100 μm away from the zero-delay line at the maximum A-line rate of 128 kHz with an incident optical power of 750 μW. The SNR roll-off in free space was measured to be ~6 dB as the optical path length difference increased from 0.1 mm to 1.2 mm. By imaging a Zeiss model eye with a 3D scan of 256×1024 A-lines, the *en-face* projection showed that the system achieved a maximum FOV of 12 mm×12 mm (Fig. 2(d), the checkerboard target printed on the back surface of the model eye has a grid size of 1mm×1mm). The measured beam size on the cornea by a scanning slit optical beam profiler (BP209-IR, Thorlabs, Newton, NJ, USA) is 2 mm, and corresponding theoretical transverse resolution is ~12μm, the actual lateral resolution on retina may be worse due to the large FOV and aberration of the eye.

2.3. Automatic focus mechanism

In OCT imaging, manually focusing tuning is typically slow and needs to subjectively decide whether the image is in the best focus, thus not suitable for efficient imaging especially

Biomedical Optics EXPRESS

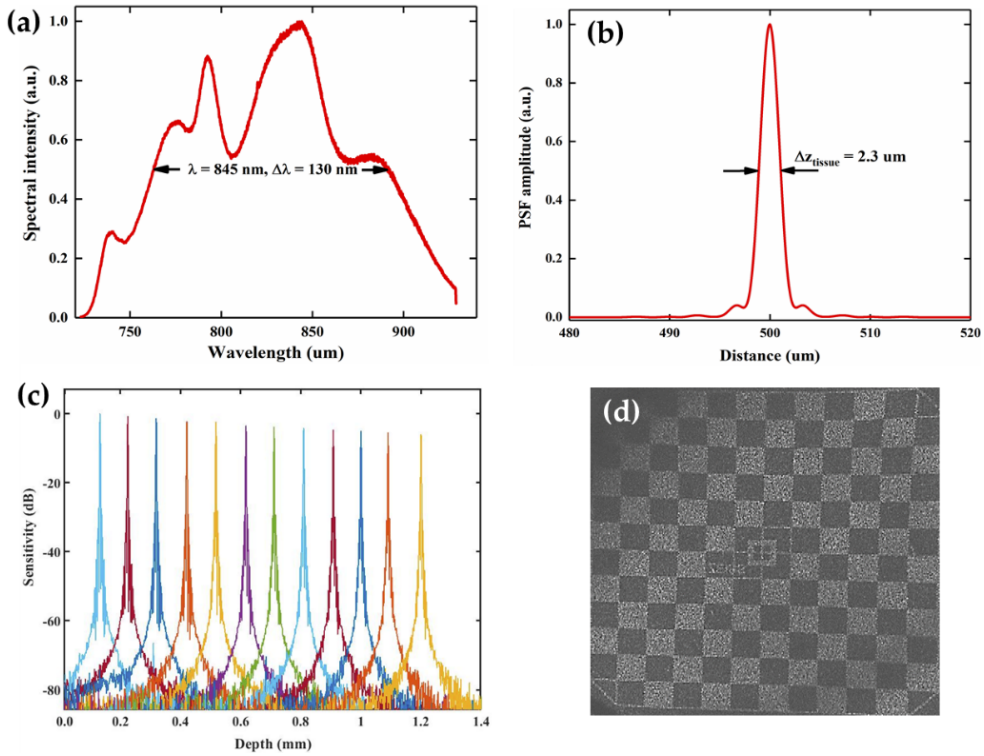

Fig. 2. System performance characterization. (a) Measured light source spectrum of the UHR-OCT system. (b) Measured axial point spread function (PSF) of the OCT system by imaging a mirror in air. (c) Measured system sensitivity roll-off. (d) The *en-face* projection image from model eye scan with maximum field of view.

when imaging uncooperative pediatric subjects. Translational stage based automatic focus tuning mechanisms are commonly used in commercial table-mounted OCT systems, but these mechanisms are usually bulky and not suitable for portable OCT systems with integrated imaging probes. The electrical lens is fast-responsive, light-weighted and does not require a long tuning range, making it suitable for our integrated imaging probe and achieving fast automatic focus [43,44]. To improve the image acquisition efficiency, we have adapted an automatic focus mechanism based on an electrical lens and a golden section search algorithm. This mechanism has been applied to a handheld OCT imaging probe before and could be referred to our former publication [45]. The effective tuning range of the electric lens is -1.5 to +3.5 diopter. During the operation, once the desired region of interest appears, the operator could use the foot switch pedal to initialize the autofocus procedure, achieving automatic focus within 1 second and the system will automatically start the image acquisition process. The automatic focusing mechanism may fail if the desired region of interest was not correctly located within the imaging range during manual adjustment or continuous eye blinking happened during the optimization process.

3. Experiments and results

To verify the performance of our customized portable boom-type UHR-OCT system, experiments were performed on healthy human subjects, sedated infants, and non-sedated awake neonates in supine position. The experimental procedures were in accordance with the tenets of the Declaration of Helsinki and were approved by the institutional review board of Zhongshan

Biomedical Optics EXPRESS

Ophthalmic Center, Sun Yat-sen University (protocol number: 2020KYPJ154). Informed consents were obtained from all the subjects or their parents. For uncooperative infants, oral chloral hydrate was applied for sedation under professional guidance. Mydriatics were used when the subjects' pupil diameter was below 3 mm. The clinical diagnosis of the subjects was made based on standard clinical examinations including indirect ophthalmoscopy.

The procedures of the OCT imaging are briefly as follows: 1) Position the device at the bedside with the probe manipulator sufficient to reach over the bed; 2) Initialize the acquisition software, set scanning parameters, adjust the imaging probe to a ready position (Fig. 3(a)), and adjust the system polarization state; 3) The subject is laid on the hospital bed or care bed with a comfortable supine position; 4) With one hand holding the imaging probe, perform initial alignment to find the pupil of the targeted eye with the iris camera image while opening the eyelids of the subject with the other hand (typically for pediatric subjects); 5) Stably adjust the probe slowly approaching the subject's eye until the OCT image of the retina appears around the middle of OCT display range, with the guidance of the real-time iris camera and *en-face* image (Figure3(b)), gently changing the direction of the examined eyeball with fingers when needed, adjust the polarization controller if significant OCT image quality damping is noticed during manipulator alignment; 6) Once confirmed ready, tread down the foot switch pedal to start the automatic focus mechanism and the image acquisition. With a well-trained operator, the total examination time would be within 10 minutes, including the system adjustment time and imaging acquisition time.

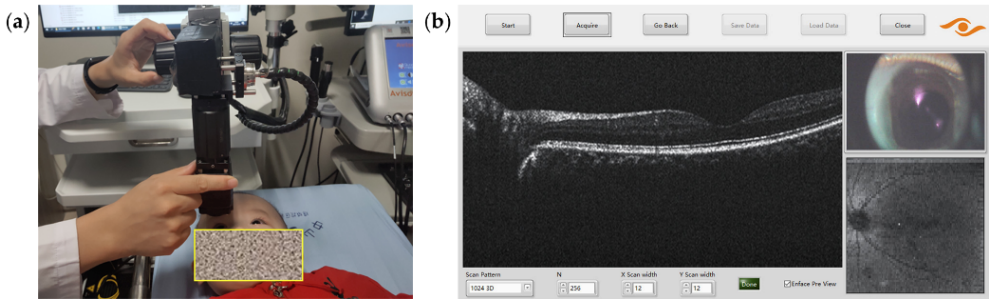

Fig. 3. (a) Picture showing the adjustment of the probe to a ready position for a non-sedated infant subject, and (b) software interface showing real-time iris camera image, cross-sectional and en face OCT images for imaging guidance.

In the experiments demonstrated in this paper, OCT images were recorded at a scan rate of 128,000 A-scans/s with a maximum scanning range of 12mm×12 mm. To identify and align the target area, real-time *en-face* view of the target area was visualized continuously. Depending on the subject and scanning mode, 2 scanning protocols were applied:

1. 3D structural OCT mode: Volumetric data is captured with 128×512 or 128×1024 A-scans within 1.5 seconds. This mode is preferred for young children and infants who are awake or subjects who have difficulty keeping their eyes fixed.

2. 2D structural OCT mode: Repeated B-scans at the same location with 2048 A-lines per B-scan are acquired. The acquisition time depends on the number of B-scans used for averaging. Normally, 5~10 B-scans requires 0.1~0.2 second. The acquired multiple B-scans are registered and averaged to improve the image quality. This mode is suitable for adults and cooperative children who could maintain a steady and fixed position, acquiring OCT images with better quality.

In this study, OCT imaging was performed in 10 awake adult volunteers and 21 infant patients (8 non-sedated and 13 sedated), achieving success rates of 91.2% on infant subjects and 100% on

Biomedical Optics EXPRESS

bedridden adults by a well-trained examiner. A successful imaging case is determined by the OCT imaging operator and an ophthalmologist upon reviewing the captured images with the criterion defined as at least one 3D volume structural scan is acquired, in which typical retinal structures like fovea, optic disc and blood vessel, or major lesions are clearly visualized. The failure cases are resulted from the lens opacity of congenital cataract and severe intraocular hemorrhage due to orbital fractures. A summary of the basic information of the imaged subjects is shown in Table 1.

Table 1. Basic information of the imaged subjects

	Adult subjects	Infant subjects
Total participants	10	21
Sex (male/female)	8/2	14/7
Age range	23 to 44 years	5 days to 40 months
Mean age	31 years	1 year and 3 months
Imaging conditions	non-sedated	non-sedated/ sedated (8/13)
Disease Condition	Healthy (20 eyes)	Healthy (11 eyes) High myopia (3 eyes) Retinal hemorrhages (3 eyes,1 failed) Retinitis (3 eye) Retinoschisis (2 eyes) FEVR (2 eyes) Cataract (2 eyes, 2 failed) ROP (2 eyes) Trauma (2 eyes) Macular hole (1 eye) RB (1 eye) LCA (1 eye) ERM (1 eye)
Total imaged eyes (success/fail)	20(20/0)	34(31/3)

3.1. Healthy adult subject

Figure 4 shows the OCT imaging results with our portable boom-type UHR-OCT on a healthy adult (29-year-old, male). 3D imaging results are shown in Fig. 4(a-c) acquired with a FOV of 9.0×9.0mm containing 512×128 pixels. Figure 4(a) shows the *en-face* average intensity projection image of the multiple B-scans, showing an overview of the retina in which typical retinal structures like fovea, optic disc and blood vessel are clearly visualized. Figure 4(b) and Fig. 4(c) are representative cross-sectional OCT images selected from the 3D volume, where Fig. 4(b) is from cross-sectional planes on the fovea and optic nerve head, demonstrating clear layer structures of the retina. Figure 4(d) shows the retinal OCT image acquired in 2D structural OCT mode by averaging 5 repeated OCT images taken at the same location, resulting in reduced speckle noise and enhanced structural details. Zoom-in areas of Fig. 4(d) are shown in Fig. 4(e) and Fig. 4(f), resolving major layer structures of the human retina, such as the retinal nerve fiber layer (RNFL), ganglion cell layer (GCL), inner plexiform layer (IPL), inner nuclear layer (INL), outer plexiform layer (OPL), outer nuclear layer (ONL), external limiting membrane (ELM),

Biomedical Optics EXPRESS

junction between inner and outer photoreceptor segments (IS/OS), end tips of photoreceptors (ETPR), retinal pigment epithelium (RPE) and Choroid.

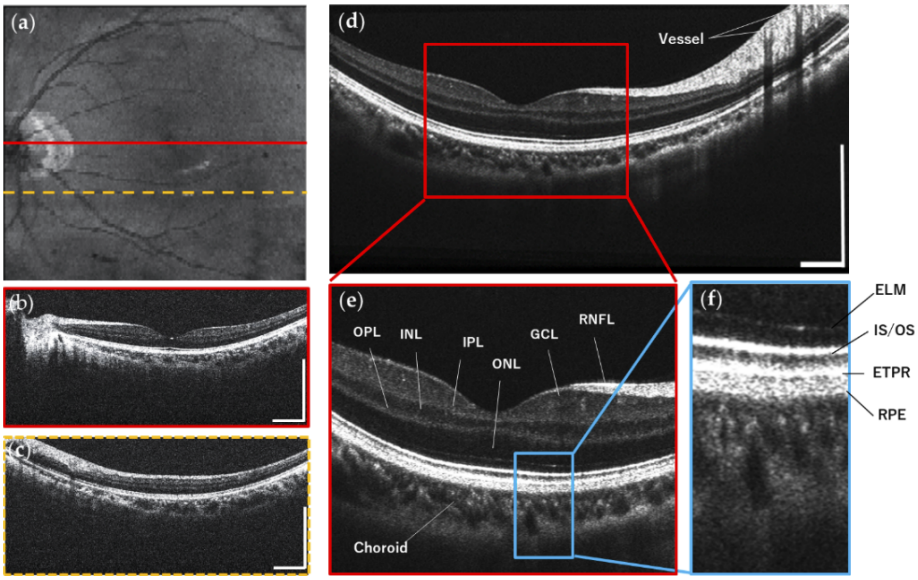

Fig. 4. Experimental results acquired from a healthy adult in supine position with our portable boom-type UHR-OCT, FOV is 9.0×9.0 mm. Structural 3D OCT imaging results are showed in (a-c): (a) *En-face* average intensity projection image of B-scans; (b) and (c) are the selected representative cross-sectional B-scans, imaging locations are indicated by lines in the *en-face* projection image. (d) The retinal OCT image acquired in 2D structural OCT mode, which was averaged from five repeated B-scans at the same location. (e) and (f) are zoom-in areas showing clear retina layer structures. RNFL: retinal nerve fiber layer, GCL: ganglion cell layer, IPL: inner plexiform layer, INL: inner nuclear layer, OPL: outer plexiform layer, ONL: outer nuclear layer, ELM: external limiting membrane, IS/OS: junction between inner and outer photoreceptor segments, ETPR: end tips of photoreceptors, RPE: retinal pigment epithelium. All scale bars: 1 mm.

3.2. *Pediatric subjects*

Figure 5 shows the experimental results demonstrated on two pediatric subjects with our OCT system both in 3D structural OCT mode with a FOV setting of 12.0×12.0mm. In magnification of retinal images, because of the short eye length and the different lateral magnification in the smaller eye, the same settings of OCT scan spans of pediatric retina images are smaller than in adults [46]. Figure 5(a-c) are the OCT imaging results acquired on a healthy eye of a sedated healthy infant (OD, 7-month-old, female), in which Fig. 5(a) is the *en-face* average intensity projection image containing 512×128 pixels, Fig. 5(b) and Fig. 5(c) are selected representative cross-sectional OCT images. The OCT images show normal retina structures of good fovea dip and clear major retinal layer structures including the RNFL, GCL, IPL, INL, OPL, ONL, IS/OS, RPE and Choroid. Figure 5(d-f) are the OCT imaging results acquired on a non-sedated and uncooperative neonate with retinoblastoma (OD, 5-day-old, male), oral chloral hydrate was not applicable for the neonate, and images were taken in non-sedated condition. The *en-face* average intensity projection image Fig. 5(d) contains 512×128 pixels, observing an obvious round shape tumor (triangle). Selected representative cross-sectional OCT images in Fig. 5(e) and Fig. 5(f) show the hyper-reflective retinoblastoma tumor (asterisk) has infiltrated into the inner retina

Biomedical Optics EXPRESS

area, and Fig. 5(e) shows the tumor has involved the macula area (arrow). Hyper reflective intra-tumoral foci of calcium (arrows) are also resolved with streak like shadowing in Fig. 5(f).

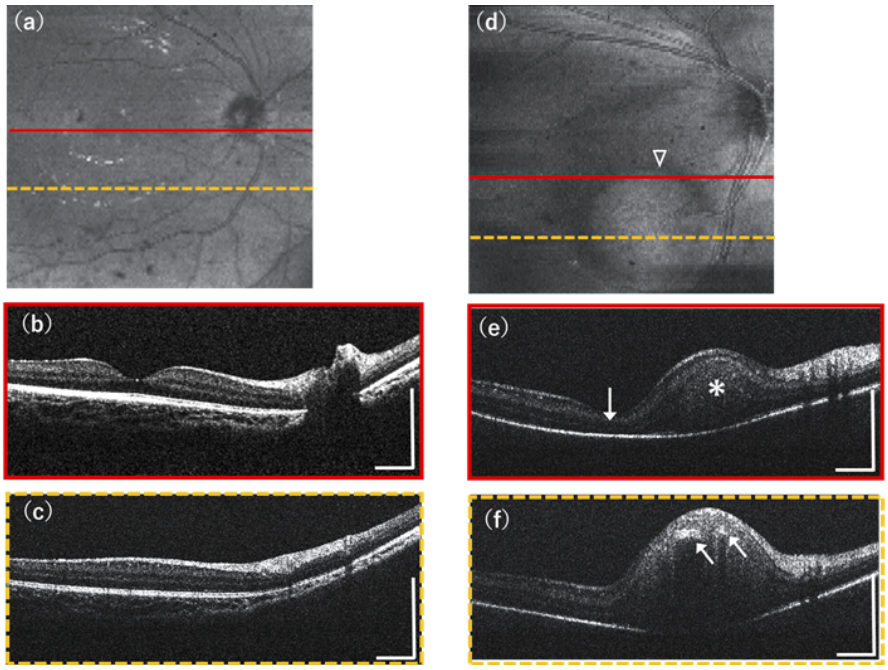

Fig. 5. Experimental results demonstrated on pediatric subjects in supine position of our portable boom-type UHR-OCT. (a-c) show the imaging results acquired from a healthy eye of a sedated infant: (a) *En-face* average intensity projection of retina, (b) and (c) are two selected representative cross-section B-scans from 3D scanning result resolving normal retinal layer structures. (d-f) are the imaging results acquired from a non-sedated awake neonate with retinoblastoma. (d) *En-face* average intensity projection image of B-scans showing a round shape tumor (triangle), (e) and (f) are selected cross-section B-scans, (e) shows the tumor (asterisk) has infiltrated the inner retina and involved the macula area (arrow), (f) shows the hyper reflective intra-tumoral foci of calcium (arrows). All scale bars: 1 mm.

Other representative imaging results acquired from infant subjects are presented in Fig. 6. Figure 6(a-b) show images acquired on eyes of a non-sedated healthy infant (OD and OS, 2-year-old, male), typical retinal structures like fovea, optic disc and major retinal layer structures are clearly visualized. Figure 6(c) shows a cross-sectional OCT image acquired from a non-sedated infant with high myopia (OD, 10-month-old, male) observing obvious retina deformation and choroidal thinning is observed (arrow). Figure 6(d) is a cross-sectional OCT image acquired from an infant patient with viral retinitis (OD, 8-month-old, female) showing intra-retinal oedema (asterisk), disruptive inner retina layers (arrow) and some degree of choriocapillaris alteration appears disrupted along the intra-retinal oedema area (triangle). The partial invisibility of the retina was due to the fact that the lesion was located at the very periphery of the retina thus the OCT beam could not fully cover the area due to the vignetting effect induced by the pupil. Figure 6(e) shows a cross-sectional OCT image from an infant patient with retinal hemorrhages (OD, 10-month-old, male), as noted by the arrows, hemorrhages appear hyper reflective and present in multiple retinal layers. Figure 6(f) shows a cross-sectional OCT image from a non-sedated infant patient with familial exudative vitreoretinopathy (FEVR) (OS, 2-year-old, male), resolving intra-retinal separation (asterisk) along with the outer nuclear layer of the

Biomedical Optics EXPRESS

retina. Figure 6(g) shows cross-sectional OCT image from an epiretinal membrane (ERM) infant patient (OS, 1-year-old, male), with local thickening of the retina (triangle), and epiretinal membrane separate from the inner retina (arrows). Figure 6(h) shows a cross-sectional OCT image from a Leber congenital amaurosis (LCA) infant patient (OS, 5-month-old, male), with upward deformation and disorganization of the retina in the macular area.

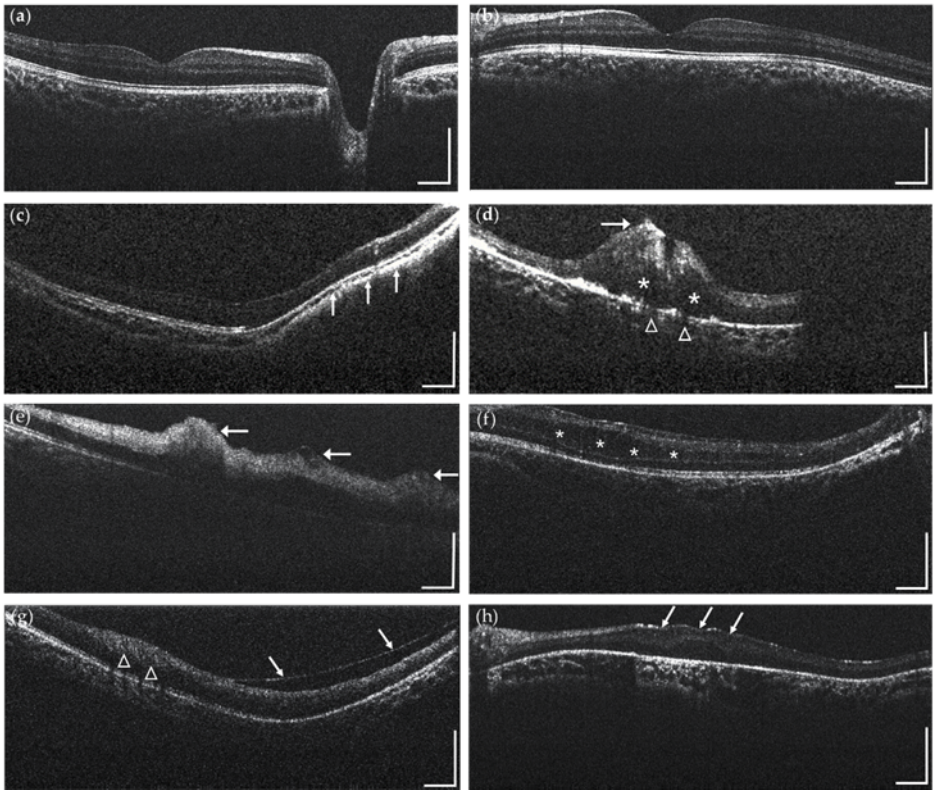

Fig. 6. Representative structural OCT imaging results obtained from pediatric patients: (a-b) healthy infant; (c) high myopia patient with retina deformation and choroidal thinning (arrow); (d) viral retinitis patient with intra-retinal oedema (asterisk), disruptive inner retina layers(arrow) and choriocapillaris alteration (triangle); (e) retinal hemorrhages patient with hemorrhages appearing hyper reflective and present in multiple retinal layers(arrow); (f) FEVR patient with intra-retinal separation (asterisk) along the outer nuclear layer of the retina. (g) ERM patient with local thickening of the retina (triangle), and epiretinal membrane separate from the inner retina (arrows); (h) LCA patient with upward deformation and disorganization of the retina in the macular area (arrows). All scale bars: 1 mm.

4. Discussion and conclusions

We have described our newly developed portable boom-type ophthalmic UHR-OCT system that can be used for in vivo non-contact high-resolution 3D imaging of retinal structures for subjects in supine position. By integrating real-time iris display and electric tunable lens into the OCT imaging probe, and coupling a self-locking multi-directional manipulator to reduce motion artifacts and operator fatigue, our device installed on a portable cart is easier for imaging alignment and more suitable for point of care imaging of subjects in supine position, especially uncooperative pediatric subjects. With a broadband SLD laser source and a high-speed

Biomedical Optics EXPRESS

spectrometer, our prototype OCT offers an axial resolution of ≈2.3μm in tissue with an A-line acquisition rate of up to 128 kHz. System feasibility has been successfully demonstrated by obtaining retinal images in healthy adults as well as sedated/awake infants.

There are several advantages of our prototype over the current commercially available armature mounted and handheld SD-OCTs, including more compact system and imaging probe design, more stable and convenient imaging procedure, and better system parameters in case of imaging speed and resolution, ensuring wider application scenarios. Table 2 shows the comparison of system specifications of our customized portable boom-type UHR-OCT system compared with the commercialized armature mounted OCT and handheld OCT systems.

Table 2. Comparison of the system specifications of our portable boom-type UHR-OCT to commercialized armature mounted OCT and handheld OCT systems.

System Specifications	Heidelberg Flex Module	Envisu C-Class	Portable Boom-type UHR-OCT
Imaging Speed (A-scan rate)	85 kHz	32 kHz	128 kHz
Axial resolution	6 μm	4 μm	2.3 μm
Volumetric scanning	-	1000×100×10/ 480×480×4	2048×1024×128 (Adjustable)
Field-of-view	55 degree	70 degree	40 degree
Probe dimensions	-	23×8×17 cm	20×8×5 cm
Imaging probe weight	-	1.6 kg	0.5 kg
Probe movement range	Horizontal:100 cm Vertical: 65 cm	Horizontal:200 cm Vertical: 200 cm	Horizontal:100 cm Vertical: 50 cm (rough); 50 mm (fine)
Probe tilt angle range	-	360 degree	360 degree
System footprint	100×100×200 cm	79×56×155 cm	50×50×140 cm
Integrated modality	OCTA/ Real-time iris display	-	Real-time iris display

Compared with the only commercialized handheld OCT system Envisu C-Class (Leica Microsystems, Germany) with a 1.6kg handheld imaging probe, our boom-type system design with a light-weighted OCT imaging probe (500g) implemented on a self-locking flexible manipulator to accommodate patients in different positions, which effectively reduces the relative motion artifacts by operator fatigue during imaging, and achieves comparable stability to table-mounted OCTs. Though the commercialized armature mounted OCT Heidelberg Flex Module (Heidelberg Engineering GmbH, Germany) has a similar boom-type configuration, it is relatively bulky and needs a space of at least 1m ×1m footprint and 2m height. Our portable system is much more compact with a footprint of 0.5m ×0.5m and a height of 1.4m, which can be easily moved around to the bedside. Moreover, researchers have shown that at least two operators were required to operate the Heidelberg Flex Module, one person for alignment, and the other to run the computer and capture the images, while in some occasions, a third person is needed to hold patients' heads still and eyelids open [46,47]. With an ergonomically designed probe installed on the self-locking flexible manipulator, our system can be operated by only one operator with one hand maintaining the probe for alignment and the other hand gently opening the eye and manipulating the eye position of the examined subjects. The incorporated multiple alignment assistant functions such as real-time direct iris viewing, automatic focusing, and *en-face* average intensity projection image visualization, also offer the operators multidimensional feedbacks that could improve the imaging efficiency and success rate. Last but not least, our system achieves higher imaging speed and better axial resolution ensuring fast and high-resolution 3D imaging

Biomedical Optics EXPRESS

on both infant and adult subjects. Indeed, the relative low scan speed of Heidelberg Flex Module (up to 85kHz A-scan rate) and Envisu C-Class (up to 32 kHz A-scan rate) have limited their 3D scan volumes and can only be applied to selected cooperative patients or infants under anesthesia who were able to tolerate the complicated imaging process [30,47]. The high-speed (up to 128 kHz A-scan rate) of our system allows high speed 3D volume scanning consisting of more than 100 B-scans even for awake infants. The ultrahigh axial resolution of 2.3μm of our system could potentially resolve more detailed structural information compared to Envisu C-Class handheld OCT (4μm) and Heidelberg Flex Module armature mounted OCT (6μm).

The high imaging speed and ultra-high axial resolution designed in our system are based on the actual clinical needs. The pediatric retinal imaging is challenging due to the fact that infant patients are usually restless with lower imaging tolerance. Their eyes are hard to maintain steady fixation during repeat scanning. Even for sedated pediatric patients, eye motions or unconscious actions do affect the imaging performance, even corrupt the successful imaging. Thus, getting images successfully as quick as possible is the first barrier of infants imaging. In these cases, lower imaging speed means more imaging artifacts and imaging failure. Using the maximum imaging speed of 128k A-scans/s, with the help of self-locking flexible manipulator, 3D volume imaging can be achieved within 1.5 seconds by our system with a reasonable SNR. While for adults and cooperative patients who could maintain a steady and fixed position, we offer the option of HD scan mode for improved image quality needs. Meanwhile, the high axial resolution are designed aiming to provide more detailed structural and functional information, which is crucial for early disease diagnosis and blindness prevention. For the infants' patients, eyes grow rapidly, and thus the microstructures undergo large developmental changes with growth. Subtle changes less than a couple of micrometers could occur in the retina during early onset and progression. Ultra-high axial resolution could benefit the detection of these tiny changes, such as hyper reflective intra-tumoral foci of calcium, and improve the visualization of photoreceptor impairment, retinal pigment epithelium (RPE) disruption, drusen, and pigment migration. With high scan speed and the reduction of hand motions and fatigue of the imaging operator using self-locking flexible manipulator, system induced image deformations were greatly reduced in our study. An internal experiment conducted by imaging a stationary model eye target and doing autocorrelation of the acquired B-scans to extract average peak-peak value of axial and lateral motions in self-locking mode (5 ± 1.1μm and 78 ± 2.4μm) have shown highly reduced motion artifacts compared to handheld mode (24 ± 5.6μm and 138 ± 3.8μm). We have also shown high imaging successful rate (91.2% on infant subjects and 100% on bedridden adults) and low deformation existence rate (13% on infant subjects and 0% on bedridden adults) in the acquired *en-face* images. The few images with deformation artifacts like discontinuities in the vessel patterns and striping were mainly due to unconscious eye movement, heartbeat or respiration happened occasionally. We believe that this low rate of deformation existence is benefited from our improved system design and should be acceptable for clinical use.

With all the above-mentioned advantages and improvements of our portable boom-type UHR-OCT system, our prototype has the potential to bring OCT system to the bedside or incubator imaging, enabling detection and monitoring of micron-level ocular conditions in pediatrics, bedridden elderly and perioperative patients. This would have a great impact on visual defeat screening and examination of these vulnerable groups, providing a new tool for improving clinical assessment and potential pathophysiological discovery.

Our system still has some limitations. Since the imaging range of SD-OCT is inversely proportional to the camera spectral resolution, the 6-dB sensitivity roll-off imaging range of our UHR-OCT system is around 1 mm. While this is sufficient for most of the retinal imaging cases as demonstrated in this study, it might be a substantial barrier to its further clinical adoption to patients with high myopia with largely curved retina. Moreover, as higher acquisition speed enables finer transverse spatial sampling of the retina, it leads to a relatively lower SNR. For the

Biomedical Optics EXPRESS

cooperative patients, the SNR could be increased with lower A-line rate and higher exposure time with increased incident power within the safety limits. But we still keep a high imaging speed with a relatively conservative incident power as most of the subjects in our study were uncooperative pediatric patients. The designed field of view of our system is relatively smaller compared with some larger FOV systems [32,34]. The FOV could be enlarged by changing the ocular lens at the end of the probe into wide-field ones. Nevertheless, these ocular lenses typically have much shorter working distances, increasing the imaging difficulties. Nevertheless, larger FOV covering peripheral retina would greatly benefit the screening of pediatric diseases like retinopathy of prematurity ROP [34,48]. Besides, although the operator hand motion and fatigue has been highly reduced, eye motions from the subject, especially the uncooperative infants, still affect the system performance. Higher imaging speed, better SNR, advanced scanning protocols and post-processing algorithms would help to achieve higher imaging quality. Since the retinal vasculature system offers crucial information for disease diagnosis and evaluation, implementing OCT angiography technique to our system would benefit in providing not only structural but also functional vascular images [47]. What is more, while multi-modal system is capable of providing adequate and comprehensive information [49–51], our system can potentially integrate other ophthalmic imaging modalities to offer additional information. Our future work would also include a large scale systematic clinical study, with a larger sample size and healthy controls.

Funding. Shenzhen Bay Laboratory (SZBL2020090501012); National Natural Science Foundation of China (81901788); Basic and Applied Basic Research Foundation of Guangdong Province (2022A1515011486); Guangzhou Municipal Science and Technology Bureau (202002030412).

Disclosures. The authors declare no conflicts of interest.

Data availability. Data underlying the results presented in this paper are not currently publicly available but may be obtained from the authors upon reasonable request.

References

1. J. G. Fujimoto, C. Pitris, S. A. Boppart, and M. E. Brezinski, "Optical coherence tomography: an emerging technology for biomedical imaging and optical biopsy," Neoplasia **2**(1-2), 9–25 (2000).
2. K. Wang, M. A. Johnstone, C. Xin, S. Song, S. Padilla, J. A. Vranka, T. S. Acott, K. Zhou, S. A. Schwaner, R. K. Wang, T. Sulchek, and C. R. Ethier, "Estimating human trabecular meshwork stiffness by numerical modeling and advanced OCT imaging," Invest. Ophthalmol. Vis. Sci. **58**(11), 4809 (2017).
3. J. Wang, Y. Xu, and S. A. Boppart, "Review of optical coherence tomography in oncology," J. Biomed. Opt. **22**(12), 1 (2017).
4. C. Posarelli, F. Sartini, G. Casini, A. Passani, M. D. Toro, G. Vella, and M. Figus, "What Is the Impact of Intraoperative Microscope-Integrated OCT in Ophthalmic Surgery? Relevant Applications and Outcomes. A Systematic Review," JCM **9**(6), 1682 (2020).
5. O. M. Carrasco-Zevallos, C. Viehland, B. Keller, M. Draelos, A. N. Kuo, C. A. Toth, and J. A. Izatt, "Review of intraoperative optical coherence tomography: technology and applications [Invited]," Biomed. Opt. Express **8**(3), 1607 (2017).
6. B. Tan, Z. Hosseinaee, L. Han, O. Kralj, L. Sorbara, and K. Bizheva, "250 kHz, 15 µm resolution SD-OCT for in-vivo cellular imaging of the human cornea," Biomed. Opt. Express **9**(12), 6569 (2018).
7. V. Mazlin, P. Xiao, J. Scholler, K. Irsch, K. Grieve, M. Fink, and A. C. Boccara, "Real-time non-contact cellular imaging and angiography of human cornea and limbus with common-path full-field/SD OCT," Nat Commun **11**(1), 1868 (2020).
8. P. Xiao, V. Mazlin, K. Grieve, J. A. Sahel, M. Fink, and A. C. Boccara, "In vivo high-resolution human retinal imaging with wavefront-correctionless full-field OCT," Optica **5**(4), 409–412 (2018).
9. Y K Ng E, J H Tan, U R Acharya, and J S Suri, *Human Eye Imaging and Modeling* (CRC Press, 2012)
10. W. Liu and H. F. Zhang, "Photoacoustic imaging of the eye: a mini review," Photoacoustics **4**(3), 112–123 (2016).
11. P. E. Napoli, M. Nioi, L. Mangoni, P. Gentile, M. Braghiroli, E. d'Aloja, and M. Fossarello, "Fourier-domain OCT imaging of the ocular surface and tear film dynamics: a review of the state of the art and an integrative model of the tear behavior during the inter-blink period and visual fixation," JCM **9**(3), 668 (2020).
12. P. Brusini, "OCT Glaucoma Staging System: a new method for retinal nerve fiber layer damage classification using spectral-domain OCT," Eye **32**(1), 113–119 (2018).
13. F. Corvi, L. Su, and S. R. Sadda, "Evaluation of the inner choroid using OCT angiography," Eye **35**(1), 110–120 (2021).
14. J. P. Kolb, W. Draxinger, J. Klee, T. Pfeiffer, M. Eibl, T. Klein, W. Wieser, and R. Huber, "Live video rate volumetric OCT imaging of the retina with multi-MHz A-scan rates," PLoS ONE **14**(3), e0213144 (2019).

Biomedical Optics EXPRESS

15. M. Wojtkowski, T. Bajraszewski, I. Gorczyńska, P. Targowski, A. Kowalczyk, W. Wasilewski, and C. Radzewicz, "Ophthalmic imaging by spectral optical coherence tomography," Am. J. Ophthalmol. **138**(3), 412–419 (2004).
16. M. D. Twa, "Ophthalmic imaging trends," Optom Vis Sci **98**(5), 427–428 (2021).
17. R. S. Maldonado and C. A. Toth, "Optical Coherence Tomography in Retinopathy of Prematurity," Clin. Perinatol. **40**(2), 271–296 (2013).
18. E. Tsui, T. A. Schempf, C. G. Besirli, N. Mehta, Y. S. Modi, G. D. Lee, and V. S. Dedania, "Imaging and testing in pediatric retina: a current review of the literature," International Ophthalmology Clinics **59**(1), 15–37 (2019).
19. S. J. Kim, A. D. Port, R. Swan, J. P. Campbell, R. V. P. Chan, and M. F. Chiang, "Retinopathy of prematurity: a review of risk factors and their clinical significance," Surv. Ophthalmol. **63**(5), 618–637 (2018).
20. "Mechanisms and Management of Retinopathy of Prematurity," N Engl J Med 368(12), 1161–1163 (2013).
21. L. S. Lim, P. Mitchell, J. M. Seddon, F. G. Holz, and T. Y. Wong, "Age-related macular degeneration," The Lancet **379**(9827), 1728–1738 (2012).
22. J. Ambati and B. J. Fowler, "Mechanisms of age-related macular degeneration," Neuron **75**(1), 26–39 (2012).
23. B. S. Gundlach and I. Tsui, "Optical coherence tomography in pediatric patients: a clinical review," Ophthalmol Eye Dis **12**, 251584142090461 (2020).
24. C. Bowes Rickman, S. Farsiu, C. A. Toth, and M. Klingeborn, "Dry age-related macular degeneration: mechanisms, therapeutic targets, and imaging," Invest. Ophthalmol. Vis. Sci. **54**(14), ORSF68 (2013).
25. C. Wu, R. A. Petersen, and D. K. VanderVeen, "RetCam imaging for retinopathy of prematurity screening," Journal of American Association for Pediatric Ophthalmology and Strabismus **10**(2), 107–111 (2006).
26. F. Chen, D. Cheng, J. Pan, C. Huang, X. Cai, Z. Tian, F. Lu, and L. Shen, "The efficacy and safety of Retcam in detecting neonatal retinal hemorrhages," BMC Ophthalmol **18**(1), 202 (2018).
27. G. Song, K. K. Chu, S. Kim, M. Crose, B. Cox, E. T. Jelly, J. N. Ulrich, and A. Wax, "First clinical application of low-cost OCT," Trans. Vis. Sci. Tech. **8**(3), 61 (2019).
28. R. Maloney, "The Optovue iVue OCT system from Grafton optical: the possibilities of hand-held OCT devices in ophthalmic practice," Journal of Visual Communication in Medicine **35**(2), 76–81 (2012).
29. C. D. Lu, M. F. Kraus, B. Potsaid, J. J. Liu, W. Choi, V. Jayaraman, A. E. Cable, J. Hornegger, J. S. Duker, and J. G. Fujimoto, "Handheld ultrahigh speed swept source optical coherence tomography instrument using a MEMS scanning mirror," Biomed. Opt. Express **5**(1), 293 (2014).
30. X. Liu, A. U. Kale, N. Capewell, N. Talbot, S. Ahmed, P. A. Keane, S. Mollan, A. Belli, R. J. Blanch, T. Veenith, and A. K. Denniston, "Optical coherence tomography (OCT) in unconscious and systemically unwell patients using a mobile OCT device: a pilot study," BMJ Open **9**(11), e030882 (2019).
31. A. Mallipatna, A. Vinekar, C. Jayadev, S. Dabir, M. Sivakumar, N. Krishnan, P. Mehta, T. Berendschot, and N. Yadav, "The use of handheld spectral domain optical coherence tomography in pediatric ophthalmology practice: Our experience of 975 infants and children," Indian J Ophthalmol **63**(7), 586 (2015).
32. S. Song, K. Zhou, J. J. Xu, Q. Zhang, S. Lyu, and R. Wang, "Development of a clinical prototype of a miniature hand-held optical coherence tomography probe for prematurity and pediatric ophthalmic imaging," Biomed. Opt. Express **10**(5), 2383 (2019).
33. C. Viehland, X. Chen, D. Tran-Viet, M. Jackson-Atogi, P. Ortiz, G. Waterman, L. Vajzovic, C. A. Toth, and J. A. Izatt, "Ergonomic handheld OCT angiography probe optimized for pediatric and supine imaging," Biomed. Opt. Express **10**(5), 2623 (2019).
34. S. Ni, T. Nguyen, R. Ng, S. Khan, S. Ostmo, Y. Jia, M. Chiang, D. Huang, J. Campbell, and Y. Jian, "105° field of view non-contact handheld swept-source optical coherence tomography," Opt. Lett. **46**(23), 5878–5881 (2021).
35. Y. Moshiri, A. Legocki, K. Zhou, M. Cabrera, K. Rezaei, K. Tarczy-Hornoch, and R. Wang, "Handheld swept-source optical coherence tomography with angiography in awake premature neonates," Quant. Imaging Med. Surg. **9**(9), 1495–1502 (2019).
36. S. Rufai, R. Bowman, C. Bunce, V. Panteli, R. McLean, S. Teli, I. Gottlob, M. Thomas, N. Jeelani, and F. Proudlock, "Feasibility and repeatability of handheld optical coherence tomography in children with craniosynostosis," Trans. Vis. Sci. Tech. **10**(8), 24 (2021).
37. G. L. Monroy and J. Won, "Clinical translation of handheld optical coherence tomography: practical considerations and recent advancements," J. Biomed. Opt **22**(12), 1 (2017).
38. X. Chen, V. Tai, B. McGeehan, G.-S. Ying, C. Viehland, R. Imperio, K. P. Winter, W. Raynor, D. Tran-Viet, S. Mangalesh, M. G. Maguire, and C. A. Tothand for the BabySTEPS Group, "Repeatability and Reproducibility of Axial and Lateral Measurements on Handheld Optical Coherence Tomography Systems Compared with Tabletop System," Trans. Vis. Sci. Tech. **9**(11), 25 (2020).
39. American National Standards Institute American National Standard for Ophthalmics—Light Hazard Protection for Ophthalmic Instruments, ANSI Z8036-2016, American National Standards Institute: New York, NY, USA,2016
40. X. Yao, K. Devarajan, R. M. Werkmeister, V. A. dos Santos, M. Ang, A. Kuo, D. W. K. Wong, J. Chua, B. Tan, V. A. Barathi, and L. Schmetterer, "In vivo corneal endothelium imaging using ultrahigh resolution OCT," Biomed. Opt. Express **10**(11), 5675 (2019).
41. D. Zhu, "Broadband superluminescent diode–based ultrahigh resolution optical coherence tomography for ophthalmic imaging," J. Biomed. Opt **16**(12), 126006 (2011).
42. D Atchison and G. Smith, *Optics of the Human Eye*, Volume 35 (Butterworth-Heinemann, 2000).

Biomedical Optics EXPRESS

43. Y. Li, P. Tang, S. Song, A. Rakymzhan, and R. K. Wang, "Electrically tunable lens integrated with optical coherence tomography angiography for cerebral blood flow imaging in deep cortical layers in mice," Opt. Lett. **44**(20), 5037 (2019).
44. J. P. Su, Y. Li, M. Tang, L. Liu, A. D. Pechauer, D. Huang, and G. Liu, "Imaging the anterior eye with dynamic-focus swept-source optical coherence tomography," J. Biomed. Opt **20**(12), 126002 (2015).
45. J. Yang, L. Liu, J. P. Campbell, D. Huang, and G. Liu, "Handheld optical coherence tomography angiography," Biomed. Opt. Express **8**(4), 2287 (2017).
46. G. Grace, H. Jeffry, H. Kenneth, S. Jonathan, C. Chris, D. Satnam, G. Melissa, and I. Will, "The Heidelberg Flex™ imaging system as a non-invasive bedside test of intracranial pressure," Invest. Ophthalmol. Visual Sci. **62**(8), 1878 (2021).
47. Y. He, M. Pettenkofer, M. G. Nittala, S. R. Sadda, I. Tsui, and A. Chu, "Early Postnatal Oxygen Exposure Predicts Choroidal Thinning in Neonates," Invest. Ophthalmol. Vis. Sci. **62**(9), 23 (2021).
48. R. S. Maldonado, J. A. Izatt, N. Sarin, D. K. Wallace, S. Freedman, C. M. Cotten, and C. A. Toth, "Optimizing hand-held spectral domain optical coherence tomography imaging for neonates, infants, and children," Invest. Ophthalmol. Vis. Sci. **51**(5), 2678 (2010).
49. P. Xiao, Z. Duan, G. Wang, Y. Deng, Q. Wang, J. Zhang, S. Liang, and J. Yuan, "Multi-modal anterior eye imager combining ultra-high resolution OCT and microvascular imaging for structural and functional evaluation of the human eye," Appl. Sci. **10**(7), 2545 (2020).
50. J. D. Malone, M. T. El-Haddad, I. Bozic, L. A. Tye, L. Majeau, N. Godbout, A. M. Rollins, C. Boudoux, K. M. Joos, S. N. Patel, and Y. K. Tao, "Simultaneous multimodal ophthalmic imaging using swept-source spectrally encoded scanning laser ophthalmoscopy and optical coherence tomography," Biomed. Opt. Express **8**(1), 193 (2017).
51. W. Song, Q. Wei, T. Liu, D. Kuai, J. M. Burke, S. Jiao, and H. F. Zhang, "Integrating photoacoustic ophthalmoscopy with scanning laser ophthalmoscopy, optical coherence tomography, and fluorescein angiography for a multimodal retinal imaging platform," J. Biomed. Opt. **17**(6), 061206 (2012).